An Overset Field-Panel Method for Unsteady Transonic Aeroelasticity

P.C. Chen[§], X.W. Gao[¥], and L. Tang[‡]

ZONA Technology*, Scottsdale, AZ, www.zonatech.com

Abstract

The overset field-panel method presented in this paper solves the integral equation of the time-linearized transonic small disturbance equation by an overset field-panel scheme for rapid transonic aeroelastic applications of complex configurations. A block-tridiagonal approximation technique is developed to greatly improve the computational efficiency to solve the large size volume-cell influence coefficient matrix. Using the high-fidelity computational Fluid Dynamics solution as the steady background flow, the present method shows that simple theories based on the small disturbance approach can yield accurate unsteady transonic flow predictions. The aerodynamic influence coefficient matrix generated by the present method can be repeatedly used in a structural design loop; rendering the present method as an ideal tool for multi-disciplinary optimization.

Introduction

The unsteady panel methods such as the Doublet Lattice Method[1] (DLM), ZONA6[2] for subsonic unsteady aerodynamics and ZONA7[3] for supersonic unsteady aerodynamics have been well accepted by the aerospace industry for many years as the primary tools for routine aeroelastic applications. The unsteady panel methods can handle complex configurations without an extensive model-generation effort, provides expedient and accurate unsteady aerodynamic predictions, and most importantly, generates the Aerodynamic Influence Coefficient (AIC) matrices that directly relate the downwash to the unsteady pressure coefficients, i.e.,

$$\{\Delta C_p\} = [AIC]\{W\} \qquad (1)$$

where ΔC_p is the unsteady pressure jumps

and W is the downwash due to the structural oscillations

The AIC matrix is considered as one of the key elements in the industrial aeroelastic design process because it is independent of the structural characteristics, therefore it needs to be computed only once and can be repeatedly used in a structural design loop.

However, it is generally believed that the unsteady panel methods are not applicable in the transonic region because of the lack of the transonic shock effects. On the other hand, the Computational Fluid Dynamic (CFD) methodology provides accurate transonic solutions by solving the Euler's or Navier-Stokes' equations, but it does not generate the AIC matrix and cannot be effectively used for routine aeroelastic applications nor for an extensive structural design/optimization. Therefore, there is a great demand from the aerospace industry to have an unsteady transonic aerodynamic method with an AIC matrix generation capability. In fact, such an unsteady transonic aerodynamic method can be developed using the unsteady field-panel method.

Integral Equations of the Unsteady Field-Panel Methods

Over the past two decades, great progress has been made in the development of the field-panel method for unsteady transonic flow computations. In 1985, Voss[4] proposed an AIC-based unsteady field panel method using a velocity potential approach. Later on, this method was improved by Lu and Voss[5] using a Transonic Doublet Lattice Method (TDLM) to eliminate the wake modeling in the velocity potential approach. The TDLM solves the so-called Time-Linearized Transonic Small Disturbance (TLTSD) equation that reads

$$\phi_{xx} + \phi_{yy} + \phi_{zz} - 2\frac{ikM_\infty^2}{\beta^2}\phi_x + \frac{k^2 M_\infty^2}{\beta^2}\phi = \frac{\partial}{\partial x}(\sigma_v) \quad (2)$$

where ϕ is the perturbed unsteady velocity potential, k is the reduced frequency, M_∞ is

the freestream Mach number, $\beta = \sqrt{1 - M_\infty^2}$, $\sigma_v = K\phi_{ox}\phi_x$. $K = \dfrac{(\gamma + 1)M_\infty^2}{\beta^2}$, and γ is the specific heat ratio.

Eq. (2) is obtained by linearizing the nonlinear transonic small disturbance equation with respect to the structural oscillating amplitude which is assumed to be small. The term ϕ_{ox} in the right hand side (RHS) of equation (2) is the steady perturbation velocity component along the freestream direction, defined here as the "steady background flow," which contains the steady nonlinear transonic shock effects in transonic flows. This is to say that the solution of equation (2) is linearly varying with the structural oscillating amplitude but it contains the nonlinear transonic shock effects embedded in the steady background flow. It should be also noted that equation (2) can lead to an AIC matrix because of its linear characteristics with respect to the structural oscillating amplitude, i.e., the downwash in the RHS of equation (1).
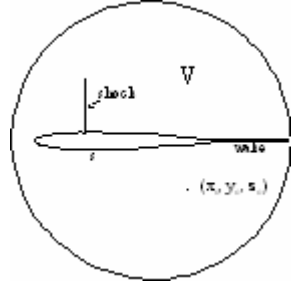
Fig. 1 Integration domain of the integral solution

Assuming $\dfrac{\partial}{\partial x}(\sigma_v)$ in the RHS of equation (2) to be a volume source, the integral solution of the TLTSD equation at a point (x_o, y_o, z_o) shown in Fig. 1 consists of three parts:

$$\phi(x_o, y_o, z_o) = \phi_s + \phi_v + \phi_{shock} \qquad (3)$$

In equation (3), ϕ_s represents the influence of the velocity potential from the surface singularities which can be written as

$$\phi_s = \frac{1}{4\pi} \iint_s \left(\frac{\Delta C_p}{2} \overline{K} - \frac{\partial \phi}{\partial n} G \right) ds \qquad (4)$$

where ΔC_p and $\dfrac{\partial \phi}{\partial n}$ are the unsteady pressure jump and unsteady source distributed on the lifting surfaces and bodies, respectively.

$\overline{K}$ is the acceleration potential kernel, whose detailed expression can be found in Ref. 2.

$$G = \frac{1}{R} e^{-\frac{ikM_\infty^2}{\beta^2}\xi} e^{-\frac{ikM_\infty}{\beta^2}R} \quad \text{is the unsteady}$$
source kernel.

and $R = \sqrt{\xi^2 + \eta^2 + \zeta^2}$, $\xi = x_o - x$, $\eta = y_o - y$, and $\zeta = z_o - z$.

In fact, equation (4) is the integral solution of the linear unsteady potential equation and is the equation solved by ZONA6 for the wing-body configurations. It should be noted that the TDLM is formulated for the lifting surface only, i.e. the unsteady source integral for bodies is absent. Here, we adopt the ZONA6 formulation to handle complex configurations such as the wing-body combinations. In the ZONA6 paneling scheme, the configuration surfaces are descritized into many small boxes, called the surface boxes, leading to a matrix that relates the surface singularity strength to the normal velocity on each box.

The second and third terms on the RHS of equation (2) read

$$\phi_v = -\frac{1}{4\pi} \iiint_V \frac{\partial}{\partial x}(\sigma_v) G dV \qquad (5)$$

$$\phi_{shock} = -\frac{1}{4\pi} \iint_{shock} \Delta\sigma_v G dS \qquad (6)$$

In equations (5) and (6), ϕ_v is the influence of the velocity potential from the volume source and ϕ_{shock} is the influence of the velocity potential from the shock surface on which $\Delta\sigma_v$ represents the jump of the volume source strength across the shock surface. Note that ϕ_{shock} automatically vanishes if the transonic shock is absent because $\Delta\sigma_v = 0$. In addition, in the presence of shock, ϕ_{shock} can be eliminated by performing integration by parts for the volume integral of ϕ_v such that

$$\phi_v = -\lim_{\varepsilon \to 0} \frac{1}{4\pi} \iint_{yz} \left\{ \int_{-\infty}^{x_s-\varepsilon} + \int_{x_s-\varepsilon}^{x_s+\varepsilon} + \int_{x_s+\varepsilon}^{\infty} \right\} \frac{\partial}{\partial x}(\sigma_v) G dx dy dz$$

$$(7)$$

gives

$$\phi_v = \lim_{\varepsilon \to 0} \frac{1}{4\pi} \iint_{yz} \sigma_v G \Big|_{x_s-\varepsilon}^{x_s+\varepsilon} dS + \frac{1}{4\pi} \iiint_V \sigma_v G_x dV \qquad (8)$$

where x_s represents the shock location and ε represents an infinitesimal thickness of the shock surface.

Combining equations (8) and (6) yields

$$\phi_{shock} + \phi_v = \frac{1}{4\pi} \iiint_V \sigma_v G_x \, dV \tag{9}$$

Equation (9) can be recast into a matrix equation by first defining a volume block surrounding the lifting surfaces or bodies and then descritizing the volume block into many small volume cells. A typical volume-cell modeling for lifting surfaces and bodies is shown in Fig. 2.

(a) Lifting Surfaces   (b) Bodies
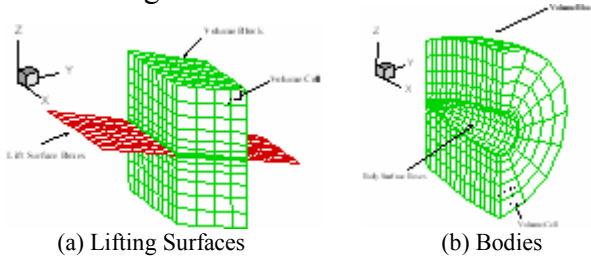
Fig. 2 Typical volume cell modeling for lifting surfaces and bodies

Unlike the CFD methodology whose volume mesh must be extended far away from the surface mesh, the domain of the volume block for the field-panel method needs only to contain the nonlinear flow region in which the volume source strength, σ_v, is significant. This is because outside the domain of the volume block the solution is dominated by equation (4), thereby the contribution from equation (9) can be ignored.

At points located on the surface boxes, the normal perturbation velocity reads

$$\{\bar{n} \cdot \bar{\nabla} \phi\} = \{W\} = [A] \left\{ \begin{array}{c} \Delta C_p \\ \dfrac{\partial \phi}{\partial n} \end{array} \right\} + [B]\{\sigma_v\} \tag{10}$$

At points located in the volume cells, the velocity potential reads

$$\{\phi\} = [C] \left\{ \begin{array}{c} \Delta C_p \\ \dfrac{\partial \phi}{\partial n} \end{array} \right\} + [D]\{\sigma_v\} \tag{11}$$

where $\bar{n} \cdot \bar{\nabla} \phi$ represents the normal perturbation velocity on the surface boxes, matrices [A] and [C] contain the influence coefficients from the surface singularities to the points on the surface boxes and in the volume cells, respectively,

and matrices [B] and [D] contain the influence coefficients from the volume sources to the points on the surface boxes and in the volume cells, respectively.

Equation (10) can be linked to equation (11) by relating σ_v to ϕ through a finite difference operator [T] such that

$$\{\sigma_v\} = [T]\{\phi\} \tag{12}$$

Voss[4] suggested that such a finite difference operator can be formulated using the Murman's scheme[6] that reads.

$$\sigma_v = (1 - \mu_i)\sigma_{vi} + \mu_{i-1}\sigma_{vi-1} + \mu_i \phi_{xi} - \mu_{i-1}\phi_{xi-1} \tag{13}$$

where $\mu_i = 0$ for $M_i < 1$ and $\mu_i = 1$ for $M_i \geq 1$, M_i is the local Mach number in the ith volume cell, and i is the index of the volume cells along the freestream direction.

The Murman's scheme is a conservative finite difference operator and guarantees the correct mathematical shock jumps. It automatically switches from the central differencing in the subsonic flows to the backward differencing in the supersonic flows, thereby, introduces the directional bias to the integral equations of TLTSD for handling the mixed flow problems of the transonic flow. The detailed expression of the matrix [T] using the Murman's scheme can be found in Ref. 7.

Substituting equation (12) into equations (10) and (11) and combining the resulting equations yields

$$\{W\} = [\bar{A}] \left\{ \begin{array}{c} \Delta C_p \\ \dfrac{\partial \phi}{\partial n} \end{array} \right\} \tag{14}$$

where

$$[\bar{A}] = [A] + [B][T][E]^{-1}[C] \tag{15}$$

and

$$[E] = [I] - [D][T] \tag{16}$$

Inverting the matrix $[\bar{A}]$ gives the AIC matrix such as the one shown in equation (1). Note that the size of the AIC matrix is only the number of surface boxes and the form of the AIC matrix is identical to that of the DLM, ZONA6, and ZONA7. This is a very attractive feature for industrial aeroelastic applications,

because once the AIC matrix is obtained, all downstream AIC-based aeroelastic solution procedures for flutter, aeroservoelastic and dynamic loads analyses remain unchanged.

However, the unsteady field-panel method does have several technical issues that need to be resolved before it can be adopted as an industrial tool for expedient unsteady aerodynamic computations.

Block-Tridiagonal Approximation of the [E] Matrix

The matrix [E] in equation (16) is a complex and fully populated matrix whose size is the number of volume cells. To model a general three-dimensional problem may require more than 10,000 volume cells and this number increases rapidly as the complexity of the configurations increases. Therefore, to invert (or decompose) such a large matrix is impractical for routine aeroelastic applications. In the present method, a block-tridiagonal approximation technique is employed to circumvent this technical issue.

The idea behind the block-tridiagonal approximation technique is a simple one. First, the volume cells are grouped into many sub-blocks. For instance, the volume blocks on the top and bottom of the lifting surface can be divided into several sub-blocks and the volume cells within the same sub-block are grouped together. In so doing, the matrix [E] can be written as

$$[E] = [E_B] + [E_\varepsilon] \tag{17}$$

where [E_B] is a block-tridiagonal matrix whose
  tridiagonal blocks contain the influence coefficients from the self-block and the adjacent sub-blocks.
  [E_ε] contains zeros in the tridiagonal blocks and the influence coefficients from the non-adjacent blocks in the off-tridiagonal blocks.

Next, by comparing the order of magnitude of the coefficients in the matrix [E_ε] to the matrix [E_B], it can be seen that all coefficients of [E_ε] are small. This is because the integrand in the integral equation shown in equation (5) contains a $1/R$ function that decays rapidly

when the point (x_o, y_o, z_o) is away from the non-adjacent sub-blocks. Therefore, the inverse of the matrix [E] can be solved approximately by the following equation:

$$[E]^{-1} \approx [E_B]^{-1} - [E_B]^{-1} [E_\varepsilon] [E_B]^{-1} \tag{18}$$

Finally, because [E_B] is block-tridiagonal, [E_B]$^{-1}$ can be computed efficiently using a block-tridiagonal matrix solver. In addition, because the block-tridiagonal matrix solver only needs to hold three block matrices in the computer memory at a time, a large amount of computer memory for solving [E]$^{-1}$ can be saved.

Overset Field-Panel Scheme for Complex Configurations

The objective of the overset field-panel scheme is to minimize the volume-cell generation effort for complex configurations. For a simple lifting surface or body shown in Fig. 2, the generation of volume cells can be automated; simply specifying the height and number of layers of the volume block. However, to generate a set of conformal volume cells over a complex configuration such as a wing with underwing stores requires an extensive volume-cell generation (or grid generation) effort.
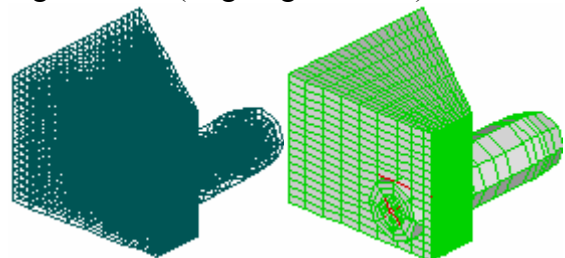
Fig. 3 Overset field-panel scheme for a wing with an underwing missile

The overset field-panel scheme allows the volume cells to be generated independently on each component of the complex configuration. For instance, a wing with a underwing missile, a pylon and fins shown in Fig. 3 can be separated into multiple components; wing, pylon, missile body, and fins. On each component, a volume block is defined independently which can be automatically divided into volume cells. Therefore, among all volume blocks volume cells of different volume blocks may intersect each other. The overset field-panel scheme constructs the influence coefficient matrices of such an

overset volume-cell model based on the following procedure:

- (a) Volume cells in different volume blocks do not influence each other.
- (b) Volume cells in the same volume block influence only their associated surface boxes.
- (c) All surface boxes influence all volume cells.

(a) One Block Modeling   (b) Overset Modeling
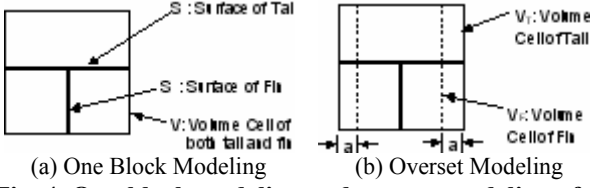
Fig. 4 One-block modeling and overset modeling of a T-tail configuration

The above overset field-panel scheme is formulated with the realization that the interference between volume blocks can be transmitted through the integral equations shown in equation (3). Unlike the overset CFD methodology where the interpolation of the flow solutions in the overset region is required, the overset field-panel scheme does not need such an interpolation. Therefore there is no need to compute the topology of the intersection among cells; greatly simplifying the volume-cell generation effort for complex configurations. To verify this scheme, let us consider a T-tail configuration consisting of a horizontal tail and a vertical fin. This T-tail configuration can be modeled by a single rectangular volume block whose volume cells are conformed to the surfaces of the tail and the fin. This one-block modeling is shown in Fig. 4.a. and its influence coefficient matrix equations read:

$$\begin{Bmatrix} W_{S_T} \\ W_{S_F} \end{Bmatrix} = [A] \begin{Bmatrix} \Delta C_{p_{S_T}} \\ \Delta C_{p_{S_F}} \end{Bmatrix} + \left[B_{VS_T}, B_{VS_F} \right] \{(\sigma_v)_v\}$$

$$\{\phi_v\} = \left[C_{S_T V}, C_{S_F V} \right] \begin{Bmatrix} \Delta C_{p_{S_T}} \\ \Delta C_{p_{S_F}} \end{Bmatrix} + [D_{vv}] \{(\sigma_v)_v\}$$

(19)

where the subscript S, S_T and S_F denote the surface boxes of the tail and of the fin, respectively.

The subscript V denotes the volume cells of the one volume block

And $(\ )_{VS_T}$ is the influence from V to S_T, $(\ )_{VS_F}$ is the influence from V to S_F, $(\ )_{S_T V}$ is the influence from S_T to V, $(\ )_{S_F V}$ is the influence from S_F to V, $(\ )_{VV}$ is the influence from V to V

Equation (19) can be considered as "exact" because of the one-block modeling. The same T-tail configuration can be also modeled by two volume blocks, one for the tail and one for the fin which are depicted by the solid box and the dashed box in Fig. 4.b, respectively. Fig. 4.b also shows that the width of the volume block of the fin is shorter than that of the tail by "2a". Apparently, the volume cells of the fin are all embedded in those of the tail; rendering a overset field-panel model. The influence coefficient matrix equations of this overset field-panel model can be written as:

$$\begin{Bmatrix} W_{S_T} \\ W_{S_F} \end{Bmatrix} = [A] \begin{Bmatrix} \Delta C_{p_{S_T}} \\ \Delta C_{p_{S_F}} \end{Bmatrix} +$$

$$\begin{bmatrix} B_{vT}{}^{S_T} & 0 \\ 0 & B_{vF}{}^{S_F} \end{bmatrix} \begin{Bmatrix} (\sigma_v)_{vT} \\ (\sigma_v)_{vF} \end{Bmatrix}$$

$$\begin{Bmatrix} \phi_{v_T} \\ \phi_{v_T} \end{Bmatrix} = \begin{bmatrix} C_{S_T} v_T & C_{S_F} v_T \\ C_{S_T} v_F & C_{S_F} v_F \end{bmatrix} \begin{Bmatrix} \Delta C_{p_{S_T}} \\ \Delta C_{p_{S_F}} \end{Bmatrix} +$$

$$\begin{bmatrix} D_{v_T v_T} & 0 \\ 0 & D_{v_F v_F} \end{bmatrix} \begin{Bmatrix} (\sigma_v)_{v_T} \\ (\sigma_v)_{v_F} \end{Bmatrix}$$

(20)

where the subscript V_T and V_F denotes the volume cells of the tail and fin, respectively.

When "a" = 0, because the domain of the tail volume block is identical to that of the fin, it is obvious that $C_{S_T V_F} = C_{S_T V_T} = C_{S_T V}$, $C_{S_F V_T} = C_{S_F V_F} = C_{S_F V}$, $B_{V_T S_T} = B_{VS_T} = B_{V_F S_F} = B_{VS_F}$ and $D_{V_T S_T} = D_{V_F S_F} = D_{VV}$, therefore $\phi_{V_T} = \phi_{V_F} = \phi_V$ and $(\sigma_v)_{v_T} = (\sigma_v)_{v_F} = (\sigma_v)_v$. Thus, the solution of the one-block modeling and the overset field-panel model is identical if "a" = 0.

When "a" $\neq 0$, the overset field-panel modeling becomes an approximation of the one-block modeling. However, because the domain of "a" is far away from the fin, its contribution of the influence to the fin is small and can be ignored as long as "a" is not very large.

The overset field-panel scheme can also greatly reduce the computer memory and CPU time for solving the [E] matrix. As shown in equation 20, because the volume cells in different volume blocks do not influence each other, the [D] matrix becomes block diagonal; leading to a block diagonal [E] matrix that can be inverted based on a block-by-block procedure. Furthermore, the block-tridiagonal approximation technique can be applied to invert each diagonal block matrix to further increase the computational efficiency.

Steady Background Flow From the High-Fidelity CFD Codes

It is well-known that the transonic small disturbance theory may not provide accurate solutions for strong transonic shock cases because it cannot correctly model the entropy gradients from strong shock nor convert the vorticity. However, this is not to say that the transonic small disturbance theory is not suitable for the prediction of unsteady flows due to small aeroelastic deformations if the total unsteady flow is decomposed into a steady background flow and an unsteady of small disturbances. As demonstrated by Liu et al.[8], simplified theories based on the small disturbance approach which can yield accurate unsteady flow predictions provided that the steady background flow on which the unsteady disturbance propagate is accurately accounted for. This suggests that, if the steady background flow in the TLTSD equation is externally provided by a high-fidelity CFD steady solution, accurate unsteady flow predictions can be ensured. This is also evident by examining the Murman's scheme shown in equation 13 where the switching scheme from the central differencing to the backward differencing is based on the local Mach numbers of the steady background flow. Thus, the unsteady shock location is dominated by

the steady shock location in the small amplitude sense; implying that accurate steady shock structures can ensure the accuracy of the unsteady shock structures.

To date, many high-fidelity CFD codes for the accurate prediction of steady flow over realistic aircraft configurations for transonic flight conditions are available. Thus, the steady background flow of the present method can be directly imported from these CFD codes. In addition, because the CFD mesh is usually much more refined than the volume cells of the field-panel method, to import the CFD steady flow solutions can be easily achieved by a simple interpolation of the CFD steady solution from the CFD mesh to the volume cells.

Validation of the Unsteady Pressure Distribution

Four test cases are selected to validate the unsteady pressure coefficients with the experimental data. The steady background flow of all four test cases are computed by the CFL3D Navier-Stokes solver[9] and interpolated to the volume cells.

F-5 wing pitching about 50% root chord at M_∞ =0.9 and k = 0.275

Fig. 5 depicts the field-panel model and the CFL3D surface mesh of a F-5 wing. The field-panel model consists of 20x10 surface boxes and 25x12x12 volume cells whereas the CFL3D mesh contains 181x77x71 grid points for the Navier-Stokes computation. The CFL3D steady pressure coefficients (Cp) at M_∞ =0.9 and angle of attack = 0º (α=0º) are first compared to the wind-tunnel measurements[10] and are shown in Fig. 6 for three span stations at y/2b = 51.5%, and = 97.7%. Excellent agreement is obtained except at y/2b = 97.7% where CFL3D slightly underpredicts the shock strength on the upper surface.
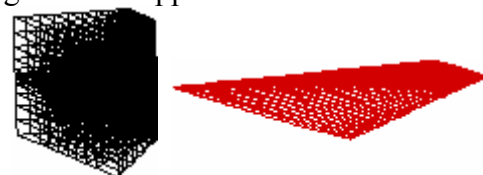
Fig. 5 Field-Panel Model & CFL3D Surface Mesh of F-5 Wing
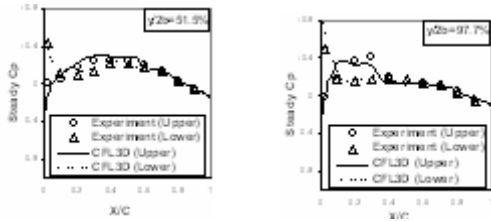
Fig. 6 Comparison of Steady Cp between CFL3D & Wind-Tunnel Results on a F-5 Wing, M$_\infty$=0.9 & α=0º
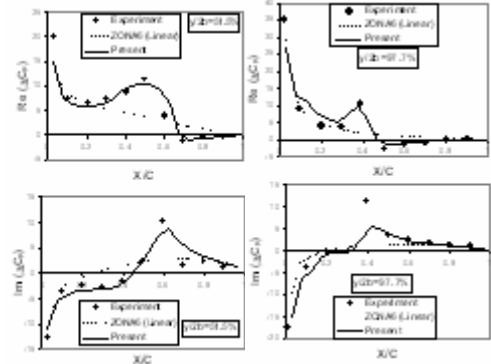
Fig. 7 Unsteady ΔCp on a F-5 Wing due to a Pitch Oscillation about 50% chord at M$_\infty$=0.9 & k=0.275

Using the CFL3D solution as the steady background flow, the unsteady ΔCp along the same three span stations computed by the present method at M$_\infty$ =0.9 and k = 0.275 due to a pitch oscillation about the 50% root chord is shown in Fig. 7. By comparing the present method to the wind-tunnel measurements, it can be seen that a good correlation is obtained except at y/2b = 97.7% where the present method underpredicts the unsteady shock strength. This is probably caused by the underprediction of the CFL3D steady shock strength y/2b = 97.7%. Also shown in Fig. 7 by the dashed line is the linear results computed by ZONA6 which fails to predict the unsteady shock effects, as expected.

LANN Wing in Pitch Mode About 62% Root Chord at M$_\infty$ = 0.822 and k = 0.105

As discussed earlier, it is generally believed that the small disturbance theories cannot give accurate aerodynamic predictions on the supercritical wings in the presence of strong shock. To show that this is not the case for the unsteady flow predictions using the present method, the unsteady pressure measurement on the LANN wing[12] is selected for validation. The LANN wing is a supercritical wing with an aspect ration = 7.92 and a 25º swept angle along ¼ chord whose field-panel model and the

CFL3D surface mesh are depicted in Fig. 13. The field-panel model of the LANN wing consists of 20x14 surface boxes and 24x16x16 volume cells whereas the CFL3D mesh contains a 269x131x71 viscous grid.

The CFL3D steady Cp at M$_\infty$ = 0.822 and α = 0.6º and at three span stations; y/2b = 47.5%, and 82.5% are compared with the wind-tunnel measured results and are shown in Fig. 14. It can be seen that the steady shock location and strength are well captured by CFL3D except at y/2b = 82.5% where the shock location on the upper surface is slightly underpredicted.

Fig. 13 Field-Panel Model and CFL3D Surface Mesh of a LANN Wing
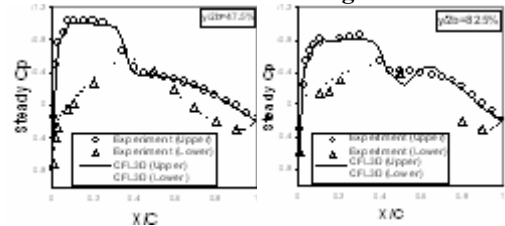
Fig. 14 Steady Cp on a LANN Wing at M$_\infty$=0.822 & α=0.6º
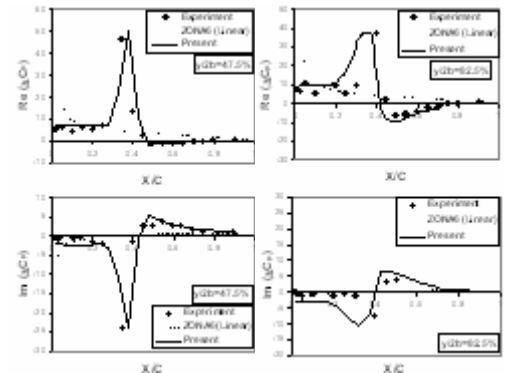
Fig 15. Unsteady ΔCp on a LANN Wing due to Pitch Oscillation about 62% Root Chord, M$_\infty$=0.822 & k=0.105

The unsteady ΔCp obtained by the present method, wind-tunnel testing, and ZONA6 on the LANN wing due to a pitch oscillation about 62% root chord at M$_\infty$ = 0.822 and k = 0.105 are presented in Fig. 15. Good agreement with the wind-tunnel results at y/2b = 47.5% is obtained by the present method. At y/2b = 82.5% the present method underestimates the unsteady shock location; again, probably due to

the underpredicted steady shock location by CFL3D. It should be noted that for this LANN wing case the ZONA6 results (dashed lines in Fig. 15) are totally unacceptable; indicating that the linear aerodynamic theories have little applicability to supercritical wings in transonic Mach numbers.

Validation of the Block-Tridiagonal Approximation Technique

The F-5 Wing at $M_\infty = 0.9$ and $k = 0.275$ case is selected to validate the block-tridiagonal approximation technique. The one-block field-panel model shown in Fig. 5 is divided into six sub-blocks along the span. Since there are 12 strips of surface boxes, each sub-block evenly occupies two strips of the surface boxes; rendering 25x12x2 volume cells in each sub-
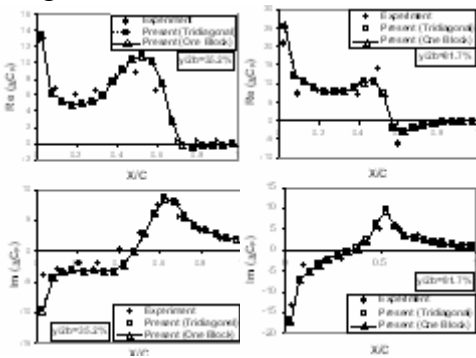
Fig. 16 Validation of the Block-Tridiagonal Approximation Technique on a F-5 Wing at M_∞=0.9 & k=0.275

block. The result of the six-sub-block model is computed using the block-tridiagonal approximation technique and compared to that of the one-block model. As seen in Fig. 16, nearly identical results between those two sets of results are obtained; showing the validity of the block-tridiagonal approximation technique. Note that the six-sub-block model gives an approximately 50% reduction in CPU time over that of the one-block model. It is believed that more significant computing time can be saved by the block-tridiagonal approximation technique for more complex configurations.

Validation of the Overset Field-Panel Scheme

The validation of the overset field-panel scheme can be performed by comparing the results between the overset modeling and the

one-block modeling. Again, we select the F-5 wing at $M_\infty = 0.9$ and $k = 0.275$ as the test case where the F-5 wing is first separated into two pieces of lifting surface (denoted as the "root section" shown in Fig. 17.a and the "tip section" shown in Fig. 17.b) along y/2b = 62.9%. Next, two volume blocks both have the full span of the F-5 wing; i.e. two identical volume blocks sharing the same three-dimensional domain, are defined for the root section and the tip section, respectively. Fig. 17.c depicts that, when joining the root section and the tip section together, an overset field-panel model of the F-5 wing is generated. According to the overset field-panel scheme, these two blocks do not influence each other and the interference between them is through the influence from the surface boxes. Because the domain of the two volume blocks is identical, there is no approximation of the overset field-panel scheme and identical result between the two-block model and the one-block model is expected.

(a) Root Section   (b) Tip Section   (c) Overset Field-Panels
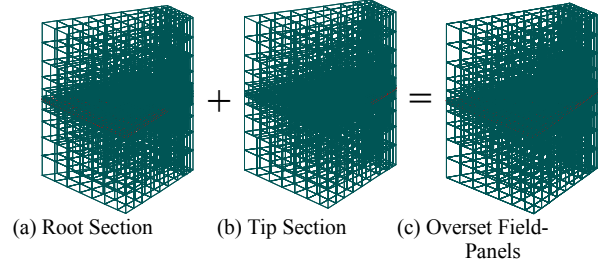
Fig. 17 Overset Field-Panel Model of a F-5 Wing with Two Volume Blocks

Indeed, as shown in Fig. 18, the result of the two-block overset model of the F-5 wing is nearly identical to that of the one-block model; verifying the mathematical "correctness" of the overset field-panel scheme.
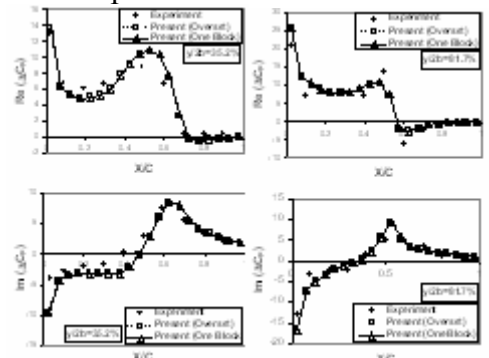
Fig. 18 Validation of the Overset Field-Panel Scheme on a F-5 Wing at $M_\infty = 0.9$ and k = 0.275

Validation of Flutter Boundary Predictions

Three test cases are selected to validate the flutter boundary prediction of the present method with the wind-tunnel measurements. Again, the steady background flows of all cases are computed using the CFL3D Navier-Stokes solver.

AGARD 445.6 Wing Flutter Boundary

The AGARD 445.6 wing[13] has two types of stiffness; the weakened wing and the solid wing; and both wings have the same aerodynamic geometry; giving an ideal case to demonstrate the AIC capability of the present method. Because the AIC matrix only depends on the aerodynamic geometry and is independent of the structural characteristics, the AIC matrix of the weakened wing can be saved and reused for the solid wing. Four AIC matrices of the weakened wing at $M_\infty = 0.678$, 0.9, 0.95, and 0.98 are first generated, whose matching flutter speed indexes $(U/_{b_s}\omega_\alpha\sqrt{\mu})$ and flutter frequencies (ω/ω_α) are shown in Fig. 19. It shows that the transonic flutter dip of a weakened wing is well predicted by the present method. Mean-while, the linear results computed by ZONA6 give a large discrepancy in the transonic region, as expected.
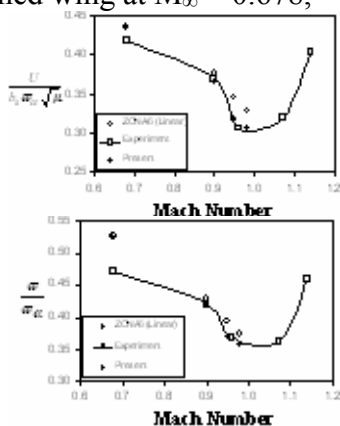
Fig. 19 Flutter Boundary of the AGARD 445.6 Weakened Wing

Fig. 20 presents the flutter boundary of the solid wing predicted by the present method but using the AIC matrices of the weakened wing. Again, good correlation with the wind-tunnel
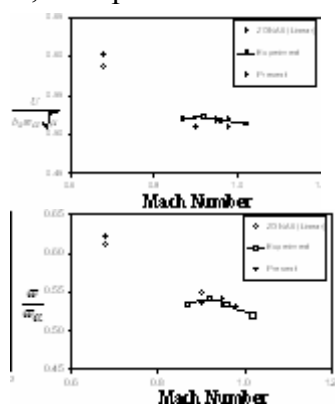
Fig. 20 Flutter Boundary of the AGARD 445.6 Solid Wing

measurements is seen. Note that the CPU time of computing the AIC matrices of six reduced frequencies at one Mach number for the weakened wing is about 3.4 hours on a 2.4 Ghz computer. Using the AIC matrices of the weakened wing, the flutter computation at four Mach numbers of the solid only takes 71secs.

Flutter Boundary of the PAPA Wing

The PAPA (Pitch And Plunge Apparatus) wing has a camber supercritical airfoil with maximum thickness of 12% and a rectangular Planform with chord of 16 inches and semi-span of 32 inches[14]. The wind-tunnel flutter test of the PAPA wing was performed in NASA/Langley's Transonic Dynamic Tunnel (TDT). The structural support of the PAPA wing provides only two modes; a plunge mode (3.43 Hz) and a pitch mode (5.44 Hz). Because of the simple structural arrangement and the complex aerodynamics due to the supercritical wing characteristics, the objective of the wind-tunnel test was to provide experimental data for the validation of aeroelastic CFD codes. However, it turns out that only a few CFD results of the PAPA wing could be found in the open literatures. This might be caused by the low-aerodynamic-damping characteristics of the PAPA wing which requires a very long computational time to determine the accurate flutter boundary using the time-marching procedure of the CFD codes[15] for transonic flutter predictions. However, this low-aerodynamic-damping characteristics is not a technical issue for the present method for flutter predictions since it is formulated in the frequency domain whose unsteady aerodynamics can be directly adopted by a frequency-domain flutter solution procedure such as the g-method[16].

Fig. 21 presents a field-panel model and a CFL3D surface mesh of the PAPA wing. The steady background flows are provided by the CFL3D Navier-Stokes solver at Mach numbers ranging from 0.5 to 0.85 and at $\alpha =1°$ and $-2°$. The CFL3D results show that at $\alpha =1°$ the transonic shock starts appearing on the upper surface at $M_\infty = 0.7$ and moves to approximately 40% chord at $M_\infty = 0.8$. At $\alpha =$

-2º, the transonic shock appears on the lower surface at $M_\infty = 0.7$ and moves to 40% chord at $M_\infty = 0.8$. These CFL3D results indicate the strong transonic effects on the PAPA wing due to its supercritical wing characteristic and present challenge to the accuracy of the flutter predictions.
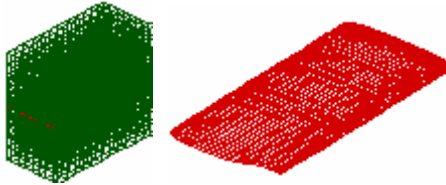
Fig. 21 Field-Panel Model and CFL3D Surface Mesh of the PAPA Wing
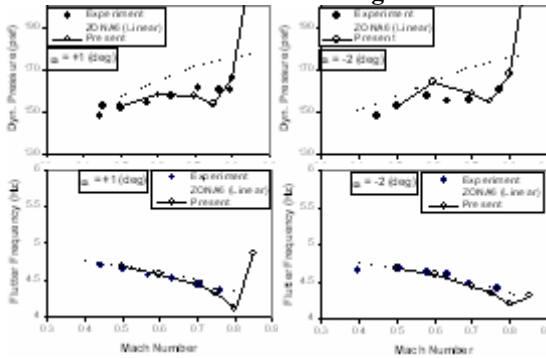
**Fig. 22 Flutter Boundaries of PAPA Wing,
α =1º(left) & -2º(right)**

The flutter boundaries at α =1º and -2º obtained by the present method, the wind-tunnel test, and the linear method (ZONA6) are presented in Fig. 22. It can be seen that the transonic flutter dips are well predicted by the present method; verifying that the present method can deal with the strong shock cases on the supercritical wings provided the steady background flow is accurately predicted by the high-fidelity CFD code such as CFL3D. Results also show that the flutter boundary of the PAPA wing in the transonic region is angle-of attack dependent. Clearly, this angle-of-attack effect on flutter boundary cannot be accounted for by the linear methods such as ZONA6. The CPU time of the present method for this case is approximately 3 hours per Mach number in a 2.4 Ghz computer.

Conclusions

An Overset field-panel method has been developed for the transonic AIC matrix generation and aeroelastic applications. The present method can be considered as a transonic counterpart of ZONA6/DLM because the surface boxes of the field-panel model can adopt those of ZONA6 or DLM. To generate the volume cells on lifting surfaces or bodies requires only a few additional input parameters such as the height and number of layers of the volume block. The overset field-panel scheme can minimize the volume cell generation efforts on complex configurations and automatically transmit the interference between overset blocks. In addition, a block-tridiagonal approximation technique is incorporated in the present method to greatly improve the computational efficiency of solving the volume-cell influence coefficient matrix that is a complex, fully populated and normally very large size matrix.

The transonic AIC matrix generated by the present method has the same form as that of the linear panel methods and can be readily plugged into any existing AIC-based aeroelastic design processes for rapid flutter, aeroservoelastic, and dynamic loads analyses. To generate an AIC matrix for a lifting surface configuration at one reduced frequency takes about a half hour of CPU time. But once generated, it can be repeatedly used in a structural design loop; rendering the present method as an ideal tool for the multi-disciplinary optimizations.

The present method also shows that simple theories based on the small disturbance approach can yield accurate unsteady transonic flow predictions if accurate steady background flow is given. This is demonstrated by the good correlation with the experimental data of the present results using the high-fidelity CFL3D Navier-Stokes solutions on the F-5 wing, the Lessing wing, the LANN wing, the AGARD 445.6 wing, and the PAPA wing.

References
1. Rodden, W.P., Giesing, J.P., and Kalam, T.P., "New Method for Nonplanar Configurations,"

AGARD Conference Proceedings, CP-80-71, Pt. II, No. 4, 1971.

2. Chen, P.C., Lee, H.W., and Liu, D.D., "Unsteady Subsonic Aerodynamics for Bodies and Wings with External Stores Including Wake Effort," *Journal of Aircraft*, Vol. 30, No. 5, Sep-Oct. 1993, pp. 618-628.

3. Chen, P.C., and Liu, D.D., "Unsteady Supersonic Computation of Arbitrary Wing-Body Configurations Including External Stores," *Journal of Aircraft*, Vol. 27, No. 2, Feb 1990, pp. 108-116.

4. Voss, R., "Calculation of 3D Unsteady Transonic Potential Flows by a Field Panel Method," *2nd Inter. Symp. on Aeroelasticity and Structural Dynamics*, Aachen, Germany, April 1-3, 1985, pp. 33-46.

5. Lu, S. and Voss, R., "TDLM-A Transonic Doublet Lattice Method for 3D potential Unsteady Transonic Flow Computation," *DLR Institut fur Aeroelastik*, Goettingen, FRG, DLR-FB 92-25, Sept. 1992.

6. Murman, E.M., "Analysis of Embedded Shock Waves Calculated by Relaxation Methods," *AIAA J.*, Vol. 12, May 1974, pp. 626-633.

7. Van Zyl, L.H., "A Transonic Doublet Lattice Method for General Configurations," *International Forum on Aeroelasticity and Structural Dynamics*, Rome, Italy, June 1997, pp. 25-31.

8. Liu, D.D., Kao, Y.F., and Fung K.Y., "An Efficient Method for Computing Unsteady Transonic Aerodynamics of Swept Wings with Control Surfaces," *J. Aircraft*, Vol. 25, No. 1, pp. 25-31, January 1988.

9. Krist, S.L., Biedron, R.T., and Rumsey, C.L., "CFL3D User's Manual." *NASA Langley Research Center*, 1997.

10. Tijdema, H., et al., "Transonic Wind-Tunnel Tests on an Oscillating Wing with External Stores," *AFFDL-TR-78-189*, Part II, Sept. 1978.

11. Lessing, H.C., Troutman, J.L., and Menees, G.P., "Experimental Determination on a Rectangular Wing Oscillating in the First Bending Mode for Mach Numbers from 0.24 to 1.30," *NASA TND-33*, December 1960.

12. Malone, J.B, and Ruo, S.Y., "LANN Wing Test Program: Acquisition and Application of Unsteady Transonic Data fro Evaluation of Three-Dimensional Computational Methods," *AFWAL-TR-83-6006*, Feb. 1983.

13. Yates, E.C., "AGARD Standard Aeroelastic Configurations for Dynamic Response I-Wing 445.6," *AGARD Report No. 765*.

14. Farmer, M.G., and Rivera, J.A., "Experimental Flutter Results of a Cambered Supercritical Wing on a Pitch and Plunge Apparatus," Presented at Aerospace Flutter and Dynamics Council Meeting, NASA Langley Research Center, May 12, 1988.

15. Private communication with John W. Edwards of NASA Langley Research Center.

16. Chen, P.C., "A Damping Perturbation Method for Flutter Solution: The g-Method," AIAA Journal, Vol. 38, No. 9, Sept. 2000, pp. 1519-1524.